ICARUS 111, 2–17 (1994)

Detection of the SO_2 Atmosphere on Io with the Hubble Space Telescope

G. E. BALLESTER

Department of Physics and Astronomy, Johns Hopkins University, Baltimore, Maryland 21218; and Department of Atmospheric, Oceanic, and Space Sciences, University of Michigan, Ann Arbor, Michigan 48109
E-mail: gilda@sunshine.sprl.umich.edu

M. A. MCGRATH

Space Telescope Science Institute, 3700 San Martin Drive, Baltimore, Maryland 21218

D. F. STROBEL[1] AND XUN ZHU

Department of Earth and Planetary Sciences, Johns Hopkins University, Baltimore, Maryland 21218

AND

P. D. FELDMAN AND H. W. MOOS

Department of Physics and Astronomy, Johns Hopkins University, Baltimore, Maryland 21218

Received October 29, 1993; revised May 2, 1994

Observations of the trailing hemisphere of Io made with the Faint Object Spectrograph of the Hubble Space Telescope in March 1992 have resulted in the first detection of atmospheric SO_2 absorption bands in the ultraviolet. These observations represent only the third positive means of detection of what is widely believed to be Io's primary atmospheric constituent. Below ~2130 Å the geometric albedo of the satellite is dominated by SO_2 gas absorption band signatures, which have been analyzed using models that include the effects of optical thickness, temperature, and spatial distribution. The disk-integrated HST data cannot resolve the spatial distribution, but it is possible to define basic properties and set constraints on the atmosphere at the time of the observations. Hemispheric atmospheres with average column density $\mathcal{N}$ = 6–10 × 10^{15} cm^{-2} and T_{gas} = 110–500 K fit the data, with preference for temperatures of ~200–250 K. Better fits are found as the atmosphere is spatially confined, with a limit of ~8% hemispheric areal coverage and $\mathcal{N} \approx 3 \times 10^{17}$ cm^{-2} with colder 110–250 K temperatures. A dense ($\mathcal{N} \geq 10^{16}$ cm^{-2}), localized component of SO_2 gas, such as that possibly associated with active volcanoes, can generate the observed spectral contrast only when the atmosphere is cold (110 K) and an extended component such as Pele is included. The combination of a dense, localized atmosphere with a tenuous component ($\mathcal{N} < 10^{16}$ cm^{-2}, either patchy or extended) also fits the data. In all cases the best fit models imply a disk-averaged column density larger than exospheric but ~10–30 times less than the previous upper limit from near-UV observations.

I. INTRODUCTION

SO_2 is to date the only molecular species positively identified in the Io atmosphere. It is of particular interest because of the unusual (and nonuniform) nature of its suspected major sources (volcanoes, sublimation of surface SO_2 frost, and sputtering), and because it plays a critical role in the origin and maintenance of the Io plasma torus via the complex interaction between satellite and plasma, thereby supplying heavy ions to the jovian magnetosphere. Despite the keen interest in what is at best an extremely tenuous atmosphere, our knowledge about the fundamental properties of its SO_2 component (especially the density, thermal structure, and areal coverage) is remarkably poor due to the difficulty in detecting it from Earth. Prior to the work described in this paper, only two means of detection of the SO_2 atmosphere have been successful in the past 15 years, and these observations have led to contradictory conclusions. The discovery detection by the Voyager Infrared Interferometer

[1] On leave at DESPA, Observatoire de Paris, 92195 Meudon Cedex, France.

Presented at the Io Conference, San Juan Capistrano Research Institute, June 1993.

0019-1035/94 $6.00

Spectrometer (IRIS) experiment of SO_2 gas absorption above the Loki hot spot was originally interpreted to imply a relatively dense ($\mathcal{N} \approx 5 \times 10^{18}$ cm^{-2}; $P \approx 1 \times 10^{-7}$ bars) atmosphere in vapor-pressure equilibrium with surface SO_2 frost (Pearl *et al.* 1979). An alternative explanation of the IRIS detection as a dense, localized SO_2 atmosphere above the Loki plume (Collins 1981) has been further supported by two subsequent studies: high-resolution, near-UV spectra obtained with the International Ultraviolet Explorer (IUE) satellite, which provided an upper limit on the hemispheric SO_2 atmospheric abundance of $\mathcal{N} \lesssim 2 \times 10^{17}$ cm^{-2} (Ballester *et al.* 1990) inconsistent with the original interpretation of the IRIS detection, and the non-LTE radiative transfer modeling of the observed IRIS absorption feature (Lellouch *et al.* 1992).

That Io's SO_2 atmosphere is nonuniform, especially with respect to the subsolar point, has always been suspected because at the effective dayside temperature of the frost, thought to range from ~90 to 130 K, the vapor pressure of SO_2 varies by four orders of magnitude (e.g., Fanale *et al.* 1982, Matson and Nash 1983, Brown and Matson 1987). In addition, the distribution of what are throught to be the main atmospheric source regions, volcanoes and bright surface regions of SO_2 frost, is highly nonuniform (McEwen *et al.* 1988). Despite this, the maintenance of a patchy SO_2 atmosphere has only recently been explored using a simplified dynamical model in which the atmospheric pressure is locally controlled (Ingersoll 1989). The large pressure gradients resulting from localized source regions would transport SO_2 gas over large distances (Ingersoll *et al.* 1985, Moreno *et al.* 1991) and this effect is enhanced by high atmospheric temperatures (Lellouch *et al.* 1992), but it seems that on Io the SO_2 flow may be curtailed to some extent, as evidenced by the lack of a more uniform SO_2 frost distribution and bright polar caps. The loss processes at play include condensation of the SO_2 gas onto cold surface regions as a cold-trap mechanism for gas flowing from the hotter areas (Fanale *et al.* 1982), dissociation by the solar UV radiation, and removal by interaction with the Io plasma torus, such as sputtering by torus ions (McGrath and Johnson 1987). Loss by subsurface cold-trapping (Matson and Nash 1983) due to the high (75–95%) porosity and lower temperature of the regolith may no longer be important, based on new infrared data indicating lower porosity (D. Matson personal communication 1993).

Millimeter-wave observations have recently provided a second means of detecting Io's SO_2 atmosphere via rotational line emission (Lellouch *et al.* 1990, 1992). Analysis of the emissions with a single component atmospheric model yielded best fits with a relatively dense but localized column of hot SO_2 gas (T = 200–600 K, P = 3–40 × 10^{-9} bars) covering only 5–22% of projected surface area. Lellouch *et al.* (1992) also found that the original Voyager picture of a dense atmospheric component smoothly distributed over the surface (such as could be produced by sublimation of a uniform coverage of SO_2 frost) did not fit their observations, in agreement with the IUE upper limit. Their results therefore support the picture of a patchy SO_2 atmosphere on Io, or at least a patchy component. Of the possible localized sublimation versus volcanic sources, Lellouch *et al.* (1992) tentatively favored the volcanic sources, since the 1991 millimeter data were fitted with a higher pressure on the trailing hemisphere than on the leading hemisphere, where the SO_2 frost coverage is more extensive (e.g., McEwen *et al.* 1988, Paresce *et al.* 1992, Sartoretti *et al.* 1994). A limitation in their analysis is that it did not include a two-component model, therefore, the role of the volcanic and sublimation components may not have been properly evaluated, since the millimeter measurements may not be sensitive to low density and/or cold atmospheric SO_2.

The absorption cross section of SO_2 peaks near 2000 Å and is at least an order of magnitude larger there than in the region near 3000 Å previously studied with IUE. Because of the higher sensitivity relative to IUE, the spectrographs on board the Hubble Space Telescope (HST) have now made the 2000-Å spectral region accessible for the first time for studies of Io's tenuous SO_2 atmosphere. We report here the first high S/N measurements of Io's reflection spectrum below ~2400 Å made with the Faint Object Spectrograph (FOS) that have yielded the third means of positive detection of atmospheric SO_2 on Io. In Section II we describe the observations and the derivation of the geometric albedo. In Section III the models for atmospheric transmission and albedo are detailed. Comparison between data and models is discussed in Section IV, with possible interpretation of the observations in terms of global or localized atmospheres at various temperatures. Finally, we summarize our results and discuss their implications in Section V.

II. OBSERVATIONS AND DATA REDUCTION

Two ~14-min exposures of Io's trailing hemisphere (~278° and ~292° orbital phase) were made on 22 March 1992 with the Faint Object Spectrograph of the Hubble Space Telescope using the blue detector and grating G190H (1573–2330 Å). The detector is a photon-counting Digicon with a linear array of 512 silicon diodes, each diode subtending 0.35″ × 1.4″, and the G190H grating operates at a dispersion of 1.47 Å/diode. We used the standard quarter-stepping strategy, which results in four samples per diode, implying significant oversampling for extended targets such as Io (~12 times per resolution element for these observations). The data have therefore been rebinned by four, and the two spectra averaged to improve signal to noise (S/N).

We used the 4.″3 × 1.″4 aperture in order to minimize throughput loss due to the spherical aberration of the telescope. Accurate centering of the satellite within this aperture was accomplished by mapping the 4.″3 × 4.″3 acquisition aperture in a series of five steps perpendicular to the dispersion direction (y) by taking a short G270H spectrum at each step (Io is too bright to be acquired using the mirror). Centering in the dispersion direction (x) is evaluated by comparing the measured wavelengths in the acquisition spectra with the known wavelengths of the strong Fraunhofer absorption lines in Io's spectrum. The measured pointing error was then corrected in real time. Our exposures required a correction of ~0.72″, with an accuracy of about half a step (0.43″), in the y direction and no correction in the x direction. A short set of confirmation measurements similar to the original acquisition described above confirmed pointing accuracy after the pointing correction uplink and prior to the science observations.

Ultraviolet FOS spectra contain a background (red leak) component consisting of near-UV and visible light instrumentally scattered to shorter wavelengths. This problem is particularly severe for late-type (e.g., solar) spectra such as those of Solar System objects. Preflight measurements of FOS instrumental scattering with the G190H grating and blue detector (Blair *et al.* 1989, Sirk and Bohlin 1985) show the scattered light to be relatively smooth, increasing linearly toward longer wavelength. FOS spectra of Io, Titan, Saturn, Uranus, and Neptune confirm the general accuracy of the preflight measurements, especially the shape of the scattered light with wavelength. The severity of the grating-scattered light scales with the flux of longer-wavelength photons. Scaling the measurements of Blair *et al.* to the level of counts in the Io data results in a shape for the scattered light that is approximately constant with wavelength. We therefore assume a constant shape with wavelength for the instrumentally scattered light in the uncalibrated Io spectrum, estimated by comparing the FOS spectrum from 1600 to 1800 Å with an average of three IUE spectra of Io's trailing hemisphere in which the instrumentally scattered light is negligible. The error involved in assuming a constant shape should only minimally affect the absolute value and large-scale structure of the derived geometric albedo, and the analysis of the atmospheric properties, based primarily on smaller scale structure, will be largely unaffected. The original and corrected FOS spectra are shown in Fig. 1. The uncertainty due to photon counting statistics of the corrected spectrum decreases from ~9% at 1975 Å to ~2% at 2130 Å, and remains at ~1.5% longward of 2130 Å. We limit our analysis to $\lambda > 1975$ Å, since appropriate SO_2 data are not available below this wavelength and the S/N of the Io spectrum decreases toward shorter wavelengths.

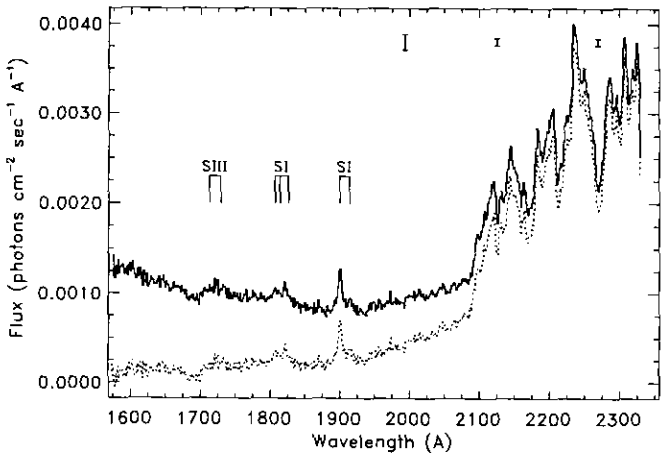

FIG. 1. The ultraviolet reflection spectrum of Io's trailing hemisphere obtained the Faint Object Spectrograph of the Hubble Space Telescope on 22 March 1992 both before (solid line) and after (dashed line) the scattered light correction described in Section 2 has been applied. Emission of neutral sulfur in Io's atmosphere and of sulfur ions in the plasma torus are also observed.

Identification of the Io atmosphere and surface contributions to the reflection spectrum requires that the structure of the solar spectrum be removed from the data. We have therefore converted the reflection spectrum to a geometric albedo, given by $p(\lambda) = F_{Io}(\lambda)\pi d^2/F_{\odot}(\lambda)\Omega_{Io}$, where F_{Io} is Io's disk-integrated flux seen from Earth, $F_{\odot}$ is the Sun's disk-integrated flux at 1 AU, d is the Io–Sun distance in AU, and Ω_{Io} is Io's solid angle as seen from Earth. (Io's 4° phase angle was set to zero for convenience.) Precise determination of the geometric albedo depends critically on use of an accurate solar spectrum, which must have the same spectral resolution as the Io spectrum. The effective resolution is determined by the FOS point spread function (PSF) for the 4.″3 × 1.″4 aperture and the apparent size of the Io disk (1.11″). The effective line spread function (LSF) was obtained by convolving the FOS PSF with a uniformly emitting disk representing Io and has a core full width at half maximum (FWHM) of ~5 Å in the dispersion direction. Perpendicular to the dispersion direction this LSF has a core FWHM of ~1.2″, which fits Io's full disk inside the aperture but results in ~15–20% loss of light in the wings due to the telescope's spherical aberration. We have convolved the solar spectrum (see below), which has higher spectral resolution than the FOS data, with the LSF derived for Io's disk. The resulting geometric albedo was then smoothed by 3 to improve the S/N.

We have chosen the Solar Ultraviolet Spectral Irradiance Monitor (SUSIM) spectrum from a Spacelab 2 experiment, which covers 1200 to 4000 Å at 1.5-Å resolution (VanHoosier *et al.* 1988) due to its accurate photometric calibration. However, this experiment had inaccuracies

in the wavelength calibration due to a mechanical failure during shuttle flight. Although the available version of the SUSIM spectrum has been corrected in wavelength with the most spectrally accurate solar spectrum available, the AFGL (Air Force Geophysics Laboratory) spectrum, obtained with a balloon-borne experiment covering 2000 to 3100 Å and accurate to ~0.04 Å in wavelength (Anderson and Hall 1989), we nonetheless found that the wavelengths of the strong solar features obvious in the Io spectrum do not match in wavelength the same features in the SUSIM spectrum. We also found the misalignment to be nonlinear. Similar problems have been reported by Clarke *et al.* (1994) and L. Trafton (personal communication) in comparisons of FOS and SUSIM spectra. Below ~2100 Å, the solar spectrum is relatively smooth and the absorption features seen in the derived albedo are quite similar, independent of the solar spectrum used. Above ~2100 Å there are many Fraunhofer absorption lines which make the derived albedo very sensitive to the spectral and photometric calibration of the solar spectrum as well as convolution with the LSF derived for Io's disk. Great care therefore had to be taken to match these features in wavelength before dividing the Io spectrum by the SUSIM spectrum to produce the geometric albedo. Relative wavelength shifts ranged from none in the 2000-2100 Å region to as large as 2.5 Å from ~2250–2330 Å.

The error in the derived albedo in the region below ~2130 Å is mainly due to statistical error in the Io spectrum since the SUSIM spectrum has very good photometric calibration and the solar spectrum should not vary much with solar activity in the UV region of interest (Lean 1987). Above ~2130 Å there is additional uncertainty arising from the nonlinear misalignment of the Io and SUSIM spectra described above. Although this misalignment has been corrected, there is still residual error involved. This wavelength-dependent error is, unfortunately, too difficult to characterize accurately.

The level of the derived geometric albedo for Io is low (Fig. 2), at the ~2% level. It is somewhat lower at 2300 Å than the geometric albedo published by Clarke *et al.* (1994), 0.022 compared with 0.027, which is derived from FOS G270H (2250–3200 Å) observations. This difference may be due to several possible things, including that the Clarke *et al.* observations were made near superior geocentric conjunction, so a different hemisphere of the satellite was observed, or that imperfect centering of Io in the aperture may move the G190H spectra partially off the detector diode array (R. Bohlin personal communication 1994). The error in the absolute level is at least the ±5% error in the SUSIM absolute photometric calibration plus the estimated ~10% for the FOS (Kinney 1992).

The spectral contrast in the derived geometric albedo is at the 10–20% level. At least eight SO_2 gas absorption bands are positively detected below 2130 Å in the derived

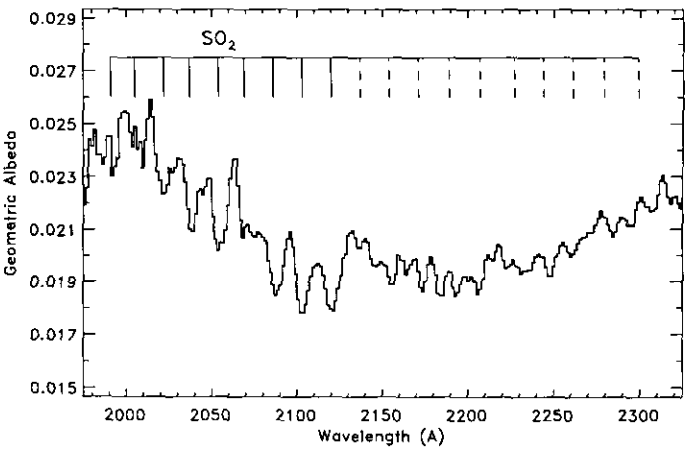

FIG. 2. Geometric albedo derived from data in Fig. 1 using the SUSIM solar spectrum. The SO_2 absorption bands of the $\tilde{C}^1B_2$–$\tilde{X}^1A_1$ system are indicated (solid ticks mark the most clearly detected bands below 2130 Å).

geometric albedo, as can be seen in Fig. 2, implying the presence of SO_2 in Io's atmosphere at column densities lower than previous detections.

III. MODELING

1. *Geometric Albedo Model and the Surface Reflectance*

The solar light reflected from Io is a function of the atmospheric transmission and surface reflectance. For the case of pure atmospheric absorption, the geometric albedo has been modeled as

$$GA(\lambda) = \frac{1}{\pi}\int_{-\pi/2}^{+\pi/2}\int_{0}^{\pi}[R_{SO_2}(\lambda)X_{SO_2}(\theta,\phi) + R_x(\lambda)X_x(\theta,\phi)] \times S^2(\lambda,\theta,\phi)\sin^2\theta\cos\phi\, d\theta\, d\phi,$$

where $S(\lambda, \theta, \phi)$ is the atmospheric transmission function described below. For the day hemisphere θ ranges from 0° to 180° and ϕ from −90° to +90°, and we have used a coarse integration grid with $\Delta\phi = \Delta\theta = 10°$.

The term in brackets represents the reflectance of the surface, for which we have assumed zero limb darkening. This is an extrapolation of the Voyager result of zero limb darkening at 3500 Å (Simonelli and Veverka 1986), and confirmation is now available from the new HST, Faint Object Camea images of Io taken with filters centered around 2300, 2600 and 2800 Å that also show no limb darkening within 20% (Sartoretti *et al.* 1994). Nonzero limb darkening could in principle affect the results derived for the hemispheric atmospheres, but not for atmospheres spatially confined near the subsolar point. Given the un-

TABLE I
Results for Fitted Model Atmospheres

Atmospheric distribution	T_{gas} (K)	T_{volcs} (K)	Column density (cm^{-2})	$\chi^2/102^a$ Weighted 1980–2130 Å	$\mathcal{S}^2/117^a$ $\times 10^{-7}$ 2130–2300 Å	$\mathcal{S}^2/219^a$ $\times 10^{-7}$ 1980–2300 Å	Range of fitted reflectance (R_x)
Atmospheres vs Column density, spatial distribution, and temperature							
Hemispheric	110	n/a	6.2×10^{15}	0.46	2.19	4.22	0.014–0.028
Hemispheric	150	n/a	5.9×10^{15}	0.37	2.14	3.34	0.014–0.028
Hemispheric	200	n/a	6.1×10^{15}	0.34	2.07	2.95	0.015–0.028
Hemispheric	250	n/a	6.6×10^{15}	0.34	2.07	2.84	0.016–0.029
Hemispheric	300	n/a	7.3×10^{15}	0.36	2.12	2.87	0.016–0.030
Hemispheric	500	n/a	1.0×10^{16}	0.52	2.41	3.33	0.017–0.032
Area ~ 50% ± 30° lat.	110	n/a	1.5×10^{16}	0.40	2.34	4.01	0.014–0.028
Area ~ 35% as frost	110	n/a	1.7×10^{16}	0.43	2.22	3.99	0.014–0.027
Area ~ 17% subsolar	110	n/a	7.4×10^{16}	0.29	2.73	3.28	0.015–0.027
Area ~ 11% subsolar	110	n/a	2.1×10^{17}	0.22	2.92	2.78	0.015–0.027
Area ~ 8% subsolar	110	n/a	3.1×10^{17}	0.31	2.32	2.63	0.014–0.026
Area ~ 5% subsolar	110	n/a	3.3×10^{17}	0.54	1.90	2.97	0.014–0.024
Area ~ 50% ± 30° lat.	250	n/a	1.5×10^{16}	0.32	2.15	2.79	0.016–0.029
Area ~ 35% as frost	250	n/a	1.8×10^{16}	0.33	2.09	2.75	0.016–0.028
Area ~ 14% subsolar	250	n/a	1.1×10^{17}	0.28	2.58	2.74	0.017–0.030
Area ~ 11% subsolar	250	n/a	1.3×10^{17}	0.35	2.28	2.75	0.016–0.029
Area ~ 8% subsolar	250	n/a	1.4×10^{17}	0.53	1.94	3.01	0.015–0.026
Area ~ 50% ± 30° lat.	500	n/a	2.7×10^{16}	0.47	2.47	3.31	0.018–0.033
Area ~ 35% as frost	500	n/a	3.0×10^{16}	0.50	2.44	3.30	0.017–0.032
Area ~ 17% subsolar	500	n/a	1.4×10^{17}	0.43	2.44	3.10	0.018–0.034
Area ~ 14% subsolar	500	n/a	1.3×10^{17}	0.54	2.15	3.16	0.018–0.031
Volcanic atmospheres							
Volcanic excl. Pele	n/a	110	$\times 10^b$	0.40	3.43	2.84	0.015–0.027
Volcanic excl. Pele	n/a	250	$\times 10^b$	0.68	4.96	3.34	0.016–0.028
Volcanic excl. Pele	n/a	500	$\times 10^b$	0.91	6.13	3.87	0.016–0.028
Volcanic incl. Pele	n/a	110	$\times 0.3^b$	0.29	2.58	2.69	0.015–0.027
Volcanic incl. Pele	n/a	250	$\times 0.1^b$	0.56	1.99	3.08	0.015–0.027
Volcanic incl. Pele	n/a	500	$\times 0.1^b$	0.83	1.90	3.66	0.015–0.027
Two-component atmospheres							
Volc. excl. Pele + Hemis	110	110	3.8×10^{15}	0.34	2.32	3.40	0.014–0.028
Volc. excl. Pele + Hemis	250	110	4.1×10^{15}	0.29	2.30	2.73	0.015–0.028
Volc. excl. Pele + Hemis	500	110	6.0×10^{15}	0.35	2.43	2.84	0.016–0.030
Volc. excl. Pele + Hemis	110	250	5.0×10^{15}	0.38	2.30	3.64	0.016–0.030
Volc. excl. Pele + Hemis	250	250	5.3×10^{15}	0.31	2.28	2.80	0.017–0.031
Volc. excl. Pele + Hemis	500	250	8.0×10^{15}	0.42	2.50	3.12	0.018–0.033
Volc. excl. Pele + Hemis	110	500	5.8×10^{15}	0.42	2.30	3.91	0.016–0.030
Volc. excl. Pele + Hemis	250	500	6.2×10^{15}	0.34	2.24	2.91	0.017–0.032
Volc. excl. Pele + Hemis	500	500	9.0×10^{15}	0.50	2.51	3.31	0.018–0.034
Volc. + Pele × 0.3 + Hemis	110	110	1.3×10^{15}	0.25	2.88	2.94	0.015–0.029
Volc. + Pele × 0.3 + Hemis	500	110	2.0×10^{15}	0.25	2.92	2.84	0.016–0.029
Volc. + Pele × 0.1 + Hemis	110	250	3.4×10^{15}	0.31	2.54	3.25	0.016–0.031
Volc. + Pele × 0.1 + Hemis	250	250	3.5×10^{15}	0.29	2.54	2.80	0.017–0.032
Volc. + Pele × 0.1 + Hemis	500	250	5.1×10^{15}	0.34	2.66	3.00	0.018–0.033
Volc. + Pele × 0.1 + Hemis	110	500	4.7×10^{15}	0.39	2.40	3.59	0.017–0.032
Volc. + Pele × 0.1 + Hemis	250	500	4.8×10^{15}	0.34	2.34	2.88	0.018–0.033
Volc. + Pele × 0.1 + Hemis	500	500	6.9×10^{15}	0.47	2.57	3.28	0.018–0.034
Comparison with results from millimeter data by Lellouch *et al.* (1990)							
1990 Trail. Hem., Area ~ 11%	200	n/a	7.2×10^{17}	0.72	3.42	4.54	0.018–0.031
1991 Trail. Hem., Area ~ 5%	350	n/a	7.2×10^{17}	1.14	1.85	4.53	0.015–0.025
Whole data Set, Area ~ 2%	600	n/a	8.2×10^{17}	1.21	1.86	4.62	0.013–0.023

[a] $\chi^2/102$ is the average sum of weighted squared differences in the region 1980–2130 Å for the best fit model densities; $\mathcal{S}^2/117$ and $\mathcal{S}^2/219$ are the corresponding average sum of squared differences over the regions 2130–2300 Å and 1980–2300 Å, respectively.

[b] Model volcanic atmospheres with original model densities or scaled by indicated factors.

certainties in this analysis, limb darkening corrections are estimated to be of minor significance.

The derived geometric albedo shows the general shape of the SO_2 frost reflectance, $R_{SO_2}(\lambda)$, as measured by Hapke *et al.* (1981) but scaled down by a factor of 0.1 to match the values measured at 2900 Å in the more detailed laboratory experiments of Nash *et al.* (1980). In this simple formulation we have assumed macroscopic mixing, although the SO_2 frost on Io may be intimately mixed (Howell *et al.* 1984, McEwen *et al.* 1988). For the spatial distribution of SO_2 frost, $X_{SO_2}(\theta, \phi)$, we have used the distribution of white frost obtained from Voyager data by McEwen *et al.* (1988) with a total areal coverage of ~35% over the trailing hemisphere and assumed that the white material is 100% SO_2 frost although this is still undetermined (Nash *et al.* 1986).

The identity of the other surface components on Io is unknown. Two other spectral end members, one of which may be sulfur, have been suggested by McEwen *et al.* (1988), but there is very little reflectance data for possible candidates below 2400 Å. We have therefore combined the reflectances of the other possible components into a single effective reflectance parameter, $R_x(\lambda)$, with a spatial distribution given by $X_x(\theta, \phi) = 1.0 - X_{SO_2}(\theta, \phi)$. $R_x(\lambda)$ is treated as a free parameter in the least-squares model fits to the observed albedo, and its range is included in the results in Table I. The fits were made in 25-Å bins, and the results were found to be insensitive to the position of the bins. For most models, the fitted reflectances $R_x(\lambda)$ are in the ~1.4–3.5% range, similar in magnitude to the reflectance used for the SO_2 frost and to the level of Io's disk-averaged albedo. We note that fitting $R_x(\lambda)$ independently for each model atmosphere makes every model agree well with the large-scale structure of the albedo. Since the abundance of SO_2 frost on Io's trailing hemisphere is low (≲35%, particularly at the subsolar point), the fitting of $R_x(\lambda)$ effectively compensates for inaccuracies in the value assigned to $R_{SO_2}(\lambda)$. The results derived for the SO_2 atmosphere are therefore mainly dependent on the modeled atmospheric transmission and the average level of Io's albedo rather than on the details of the model surface reflectance or the large-scale structure of the albedo.

2. *Model of Atmospheric SO_2 Band Absorption*

For the model transmission of the atmosphere we have only included SO_2. Of the other possible atmospheric components only the dissociation product SO has absorption bands in the UV region of interest, but these bands do not correspond to the absorption signature in Io's albedo.

The SO_2 atmospheric transmission S and absorption A over a narrow frequency band $\Delta\nu$ can be written as

$$S = \frac{1}{\Delta\nu}\int_{\Delta\nu} \exp(-\sigma_\nu \mathcal{N})\, d\nu \sim \frac{1}{\Delta\nu}\sum_{i=1}^{M} \exp(-\sigma_i \mathcal{N})\, \Delta\nu_i, \quad (1)$$

where $\mathcal{N}$ is the SO_2 column density, and

$$A = 1 - S. \quad (2)$$

For an absorption cross section σ_ν that only varies slightly within the frequency band $\Delta\nu$, the band absorption can be calculated by Beer's law, i.e., by setting $M = 1$ and $\sigma_\nu = \bar{\sigma}$ in (1), where $\bar{\sigma}$ is the mean cross section. When σ_ν varies significantly within $\Delta\nu$, the use of Beer's law over the whole band ($M = 1$) can lead to significant underestimates of absorber abundance when line saturation occurs, as pointed out by Belton (1982). For the spectral region of our HST observations this situation is applicable to SO_2 band absorption because according to the laboratory data of Freeman *et al.* (1984) the magnitude of σ_ν varies more than a factor of 10 in the model spectral intervals. The most accurate method of calculating the band transmission is an exact integration of (1) in which M is set large enough to evaluate the frequency integration exactly. However, such an approach will be very time consuming if the spectrum is composed of many lines having different line intensities so that σ_ν varies rapidly with ν. A more efficient way to incorporate the curve of growth for a band composed of many lines is to use random band models for band transmission in which forms of line profile and line intensity distribution are specified (Goody and Yung 1989). For SO_2 at low pressure and temperature the atmospheric transmission should be modeled with either Doppler or Voigt line profiles because the Voigt parameter, defined as $2\alpha_L/\alpha_D$, is at most 0.01, where α_L and α_D are, respectively, the natural and Doppler half-widths. Generally, there are no available closed expressions for band transmission with Doppler line profiles that cover both short and long absorption paths (Goody and Yung 1989). For a Voigt line profile Zhu (1988) derived several closed expressions for the band transmission. However, to apply the random band model, spectral parameters such as line intensity and line half-width for each line are required in order to effectively determine the corresponding spectral parameters that describe the statistical properties of the line intensity distribution (Zhu 1991).

The Freeman *et al.* (1984) laboratory data were acquired photographically at a resolution $(\delta\lambda)_{instr}/\lambda \approx 3 \times 10^{-6}$ and photoelectrically at a resolution $(\delta\lambda)_{instr}/\lambda \approx 1 \times 10^{-5}$, which may be compared to the ratio $(\delta\lambda)_{Doppler}/\lambda \approx 3 \times 10^{-6}$. Thus, individual rotational lines were not resolved in this experiment, but the spectral parameters can still be determined by noting the following. Freeman *et al.* state that "At energies below ~51,000 cm^{-1} (1960 Å), the

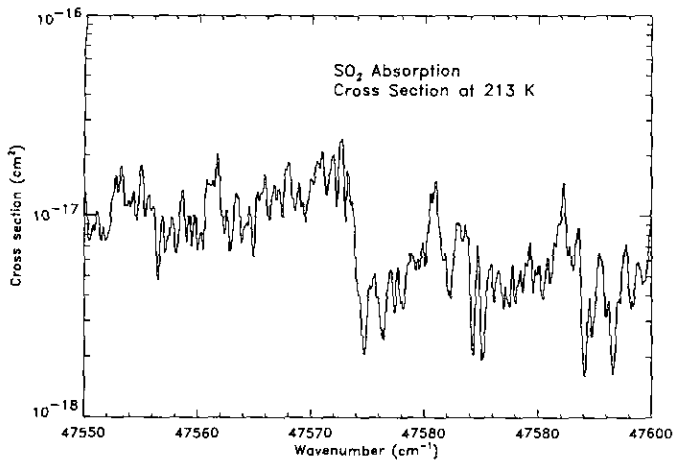

FIG. 3. High-resolution absorption cross section of SO_2 over $\Delta\lambda$ = (2100.8, 2103.0) Å at T = 213 K (from Freeman *et al.* 1984).

measured cross sections are probably close to absolute because the spectral features being measured are often not individual rotational lines of Doppler width (FWHM) ~0.06 cm^{-1}, but clusters of overlapping lines; etc...." Although the lines are Doppler, when they are overlapping the important property is the envelope of line clusters rather than individual properties of the line. The distinction among Doppler, Voigt, and Lorentz lines vanishes with significant line overlap; only the cluster envelope needs to be accurately modeled. This provides us with an opportunity to model a set of Voigt lines by a set of Lorentz lines whose expression for the band transmission is extremely simple when a Malkmus distribution is adopted for the line intensity distribution. Two spectral parameters in the Malkmus model can be determined by minimizing the difference of the absorption between the analytical model and the exact evaluation of (1) based on the experimental data from Freeman *et al.* (1984). A more efficient technique that also has a clear physical basis for the determination of the spectral parameters in the Malkmus model is through the recently developed k-distribution methods (Goody and Yung 1989, Lacis and Oinas 1991, Zhu 1994).

From the expression for the band transmission (Eq. (1)) we see that it is not important where in $\Delta\nu$ a particular value of σ_i is located. The absorption by σ_i only depends on the fraction of frequency range that $\Delta\nu_i$ occupies. Thus the absorption cross section in frequency space can be sorted according to the absorption strength and labeled with a normalized frequency variable g (Figs. 3 and 4). The band transmission can be computed in the g variable by

$$S = \int_0^1 \exp(-k_g \mathcal{N})\, dg \sim \sum_{j=1}^{L} \exp(-k_j \mathcal{N})\, \Delta g_j. \tag{3}$$

Because the sorted k-distribution k_g is much smoother than σ_ν, L can be much smaller than M to yield a relatively accurate band absorption. In the example shown by Figs. 3 and 4 for which M = 578 we obtain the band absorption (Fig. 5) with a fractional error of less than 2% with L = 10 (Fig. 6).

For any given random band model there exists a corresponding k-distribution that yields the same band transmission. Here we adopt the following widely used Malkmus model for SO_2 band transmission (Goody and Yung 1989) whose k-distribution is also known

$$S = \exp\left(-\frac{\pi}{2}\, y\left[\left(1 + \frac{4\bar{\sigma}}{\pi y}\mathcal{N}\right)^{1/2} - 1\right]\right), \tag{4}$$

where $\bar{\sigma}$ is the mean cross section

$$\bar{\sigma} = \frac{1}{\Delta\nu}\int_{\Delta\nu} \sigma_\nu\, d\nu = \frac{1}{\Delta\nu}\sum_{i=1}^{M} \sigma_i\, \Delta\nu_i. \tag{5}$$

The corresponding k distribution for (4) is given by (Lacis and Oinas 1991, Zhu 1992)

$$g(k) = \frac{1}{2}\{e^{\pi y}\ \mathrm{erfc}[(\sqrt{\pi y}/2)(\sqrt{1/\kappa} + \sqrt{\kappa})] + \mathrm{erfc}[(\sqrt{\pi y}/2)(\sqrt{1/\kappa} - \sqrt{\kappa})]\}, \tag{6}$$

where $\mathrm{erfc}(x)$ is the complementary error function and κ is the dimensionless k-coefficient $\kappa = k/\bar{\sigma}$. The parameter y in (4) and (6) has been determined by two different methods. When all the lines are pure Lorentzian then $y = \alpha_L/\delta$ is proportional to the ratio of the mean Lo-

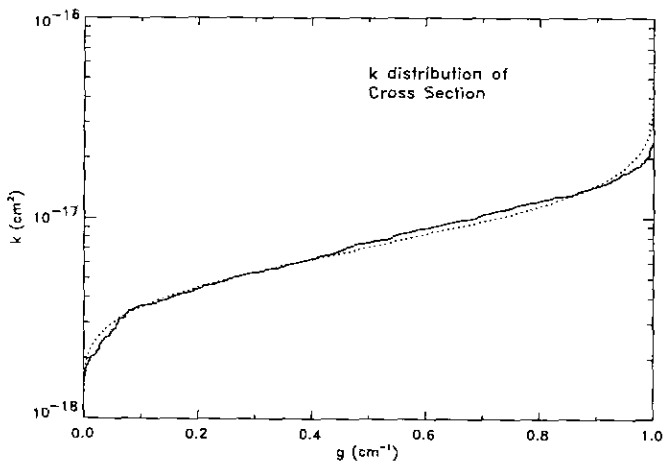

FIG. 4. The k-distribution of Fig. 3 (solid line) and the corresponding k-distribution of the Malkmus model (dotted line) derived from a least-squares fit.

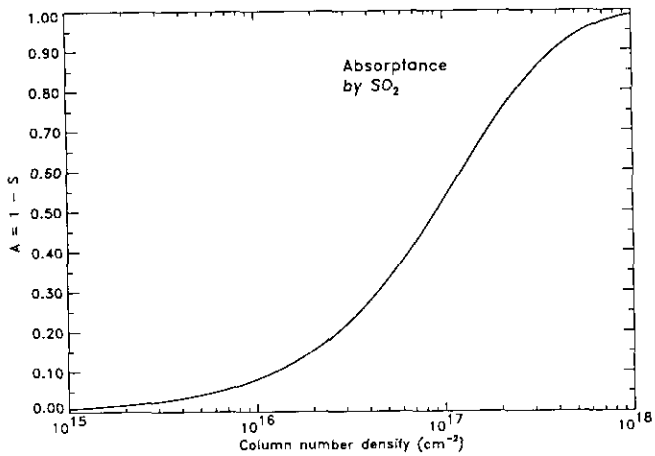

FIG. 5. The absorptance calculated by the absorption cross section shown in Fig. 3 and using Eq. (1) with $M = 578$.

rentzian half-width α_L to the mean line spacing δ (Goody and Yung 1989, Zhu 1991). When the Doppler effect becomes important or the individual lines are not resolved in a given spectrum, y can be better determined by least-squares fitting the band transmission (4) to the exactly integrated transmission (1) (Lacis and Oinas 1991). This second procedure requires performing, many times, repeated high-resolution integrations of (1) for a set of values of absorber amount ranging from weak absorption to strong absorption. However, if the parameter y is determined by a third method, i.e., a least-squares fit between the exact k-distribution and the Malkmus model (Eq. (6)), we have to perform only the high-resolution integration once to compute the exact k-distribution (Fig. 4). With the one-to-one correspondence relation between the k-distribution and band transmission we expect expression (4) with two band parameters $\bar{\sigma}$ and y determined by the third method to yield a good approximation for the band absorption. In our example (Fig. 4) two curves of different k distributions are well fitted with $\bar{\sigma} = 8.3912 \times 10^{18}$ cm^{-2} and $y = 1.8478$. The fractional errors in absorption given by (4) are less than 2% and comparable to the result obtained with $L = 10$ in Eq. (3) (Fig. 6).

The Malkmus model (4) is applied to narrow-band spectral intervals, $\Delta\lambda$, to calculate individual band transmission in each interval

$$S(\lambda) = \exp\left(-\frac{\pi y(\lambda)}{2}\left[\left(1+\frac{4\bar{\sigma}(\lambda)}{\pi y(\lambda)}\mathcal{N}\right)^{1/2}-1\right]\right) \quad \text{for each } \Delta\lambda \quad (7)$$

$$S(\lambda) \to \exp(-\bar{\sigma}(\lambda)\mathcal{N}) \quad \mathcal{N} \to 0: \quad (8a)$$

$$S(\lambda) \to \exp(-[\pi y(\lambda)\bar{\sigma}(\lambda)\mathcal{N}]^{1/2}) \quad \mathcal{N} \to \infty, \quad (8b)$$

where (8a) and (8b) are the asymptotic limits for small column densities (optically thin limit) and large column densities (optically thick limit), respectively. The parameters $y(\lambda)$ and $\bar{\sigma}(\lambda)$ were derived with SO_2 laboratory data of high spectral resolution (0.004 Å) obtained at 213 K (Freeman *et al.* 1984). The parameter $y(\lambda)$ was fitted as a function of wavelength from the laboratory data and for the $\Delta\lambda$ sampling range of the FOS data (1.47 Å), and was found to be greater than 1 in many cases. This fact implies that there is a considerable overlap among the closely packed rotational lines so that pseudocontinuum spectra are formed in those bands. From (4) we note that such a pseudocontinuum spectrum with $y \gg 1$ prevents curve-of-growth effects from becoming important until much larger optical thicknesses ($\bar{\sigma}\mathcal{N}/y \gg 1$) are attained.

The temperature dependence of SO_2 band absorption was also modeled since analysis of the millimeter-wave observations has yielded a relatively hot (200–600 K) SO_2 atmospheric component (Lellouch *et al.* 1992), and Io's surface temperature is cold (<130 K). In addition to the Freeman *et al.* (1984) data, we used SO_2 gas absorption cross sections above 1975 Å obtained at 300 K with 1-Å spectral resolution by Martinez and Joens (1992) to derive a temperature dependence assuming the usual function form $\bar{\sigma}(\lambda) = [\sigma_0(\lambda)/T]\exp[-B(\lambda)/T]$, with B derived from comparison of the 213 and 300 K data. Figure 7 shows the SO_2 absorption cross section behavior of our random band model for gas temperature 110, 250, and 500 K, showing how the contrast is more pronounced at lower temperatures and how the absorption peaks and the skewness of the bands shift to the right (i.e., longer wavelengths) at higher temperatures.

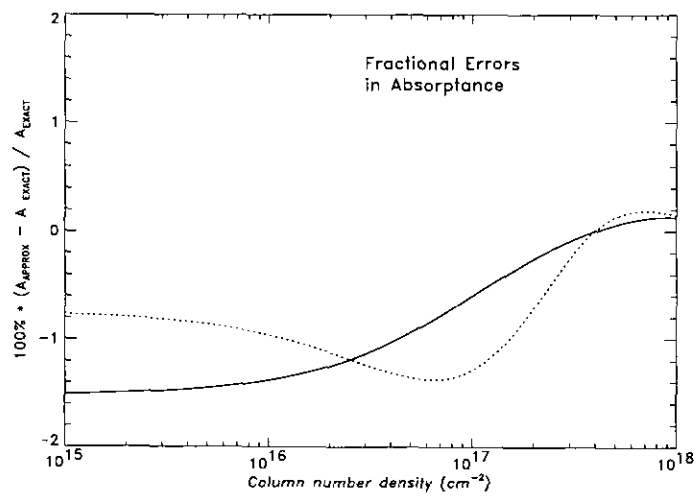

FIG. 6. Fractional errors in absorptance. The solid line is the error by using Eq. (3) with $L = 10$ and $\Delta g_j = 0.1$. The dotted line is the error by using the Malkmus model (Eq. (4)) with $\bar{\sigma} = 839 \times 10^{-18}$ cm^2 and $y = 1.85$.

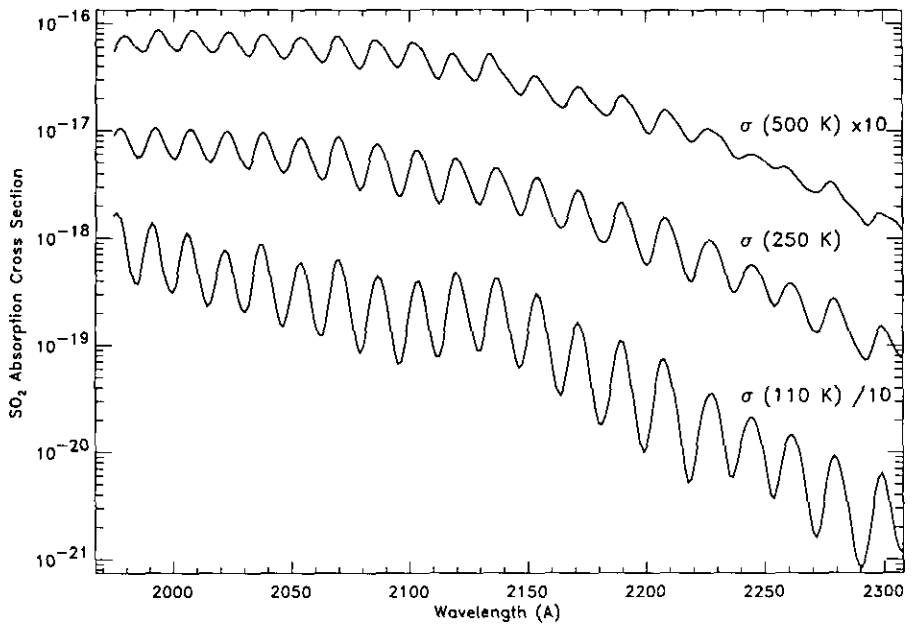

FIG. 7. The SO_2 absorption cross section at different temperatures, illustrating the band depth and band skewness effects. The curve for 500 (110) K has been multiplied (divided) by 10.

IV. COMPARISON BETWEEN DATA AND MODELS

1. Fitting Method

The geometric albedo derived for Io with the HST data can be separated at 2130 Å into two regions. Below 2130 Å the error in the albedo is dominated by the statistical error in Io's spectrum, and in this region the SO_2 absorption bands are strong. Above 2130 Å, where the SO_2 bands are weaker, there is additional, undetermined error due to nonlinear misalignments in the prominent Fraunhofer lines of the solar and Io spectra that complicates the model fitting in this region (Section II). As described below, we had to develop two different fitting methods to analyze the data. The results were relatively similar, and only those from the second method are presented in the paper.

The first method consisted of a nonweighted, least-squares model fit to the data covering the whole spectral region 1980–2300 Å. Figure 8 shows the result obtained with this method for a hemispheric atmosphere at 250 K with best fit column density of 4.7×10^{15} cm^{-2} (the results are discussed below). This figure also includes model albedos for the same atmosphere with the column density scaled by a factor of 2, showing that the spectral contrast of the SO_2 absorption bands is sensitive to SO_2 column density to better than a factor of 2. The problem encountered with this general, nonweighted method is that the fits are "pulled" by the region above 2130 Å and the contrast of the SO_2 bands below 2130 Å is not as large as that apparent in the data. This point will be more evident in the discussion of Fig. 10.

The second method results in better contrast in the SO_2 bands below 2130 Å and consists of a least-squares fit weighted by the statistical error in the region 1980–2130 Å. The quality of the fit is estimated by the weighted sum

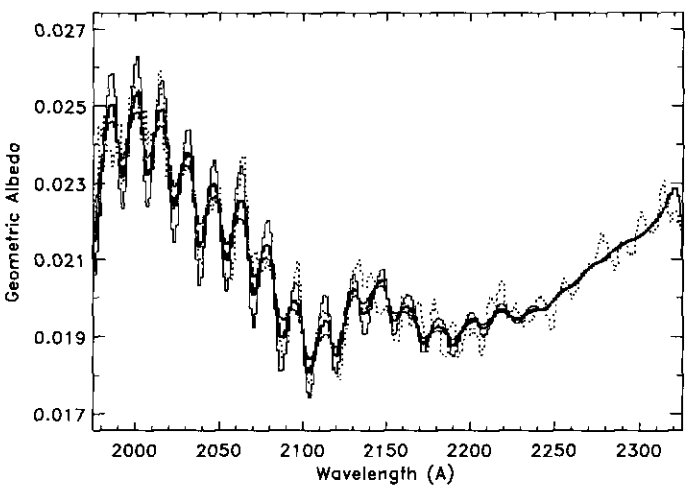

FIG. 8. Results with the nonweighted, least-squares fitting method over the whole spectral region 1980–2300 Å for a hemispheric SO_2 atmosphere at 250 K with the observational data of Fig. 2. Short-dashed line, data. Thick solid line, best fit with column density of 4.7×10^{15} cm^{-2}. Thin solid lines, model albedos for the same atmosphere with the column density scaled up (down) by a factor of 2 showing larger (smaller) spectral contrast.

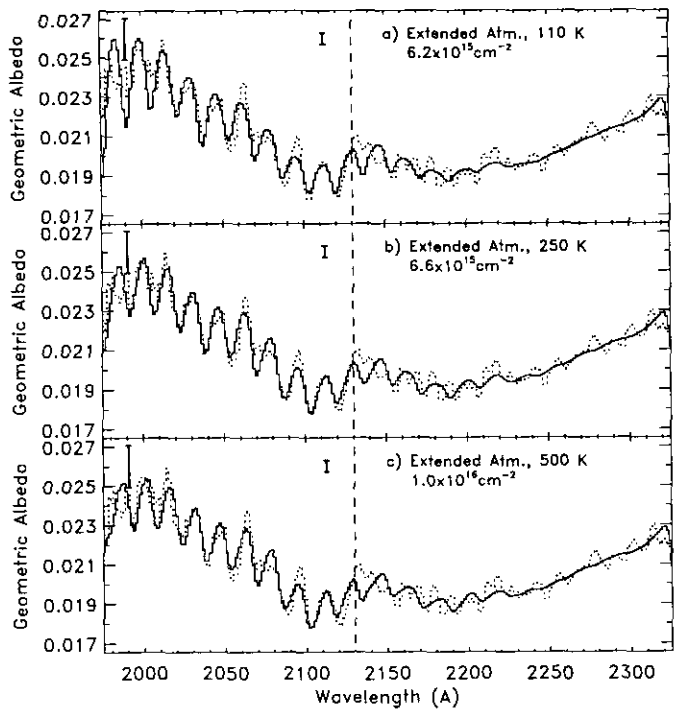

FIG. 9. Comparison between best fit models of hemispheric atmospheres at different temperatures with the observational data of Fig. 2. Solid lines, model albedos. Short-dashed line, data. (a) 110 K. (b) 250 K. (c) 500 K.

of square differences between fit and data divided by the number of data points, $\chi^2/102$. The result for the example case of the hemispheric atmosphere at 250 K is presented in Fig. 9b, showing that the right level of contrast is fitted for the SO_2 bands below 2130 Å. The fitted column density is 6.6×10^{15} cm^{-2}, 1.4 times higher than found with the first fitting method, confirming that the error in these fits is better than a factor of two. The region above 2130 Å is also taken into consideration by: (i) checking how the best fit for the region below 2130 Å compares with the data above 2130 Å using the average sum of squared differences, $\mathcal{S}^2/117$; (ii) by evaluating the corresponding average sum of squared differences for the full spectral region 1980–2300 Å, $\mathcal{S}^2/219$, to represent the overall fit to the data, and; (iii) by visual inspection. Rigorously, however, we cannot define a limit for an acceptable contrast above 2130 Å because we do not know what the errors are in this region. As can be seen in Figs. 8, 9, and others presented below, this region is not fitted acceptably by any of the models; some SO_2 bands are out of phase with the albedo. A more accurate solar spectrum would be invaluable in understanding this portion of Io's reflection spectrum.

The weighted-fitting method was selected for the analysis of the HST data presented: the results and

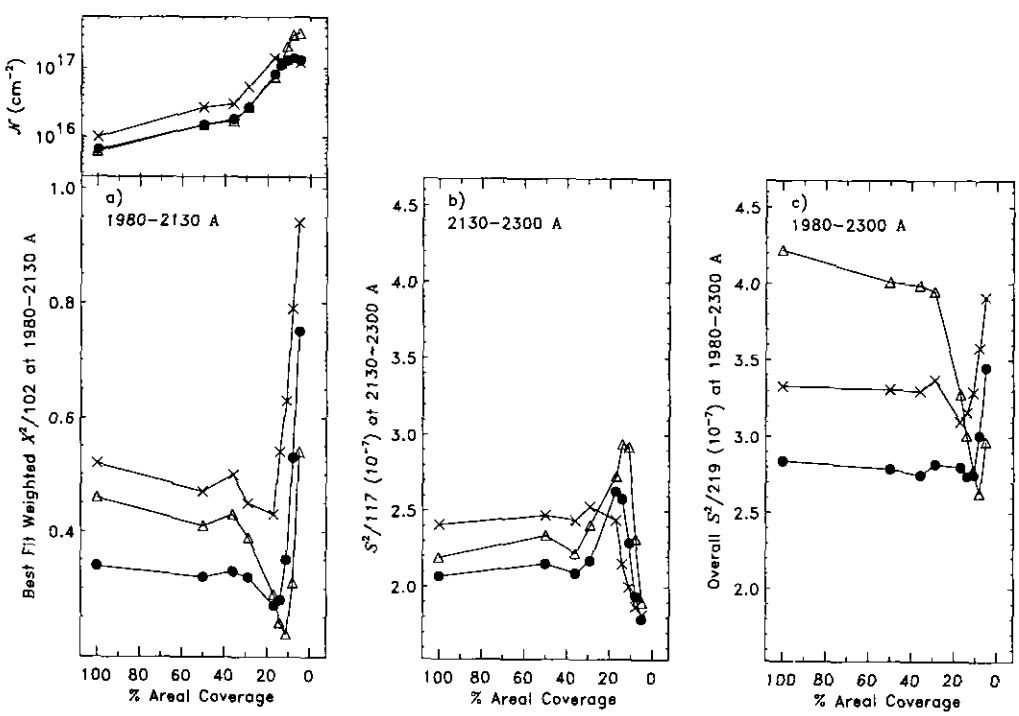

FIG. 10. Results on the role of SO_2 column density, spatial distribution and temperature. Triangles T = 110 K. Solid circles T = 250 K. Crosses T = 500 K. (a) Average weighted sum of squared differences for the region 1980–2130 Å ($\chi^2/102$) for the best density fits versus the percent areal coverage for gas at the three temperatures. The derived column densities are plotted on the top panel. (b) Corresponding average sum of squared differences (nonweighted) over the region above 2130 Å ($\mathcal{S}^2/117$). (c) Corresponding average sum of squared differences ($\mathcal{S}^2/219$) over the full spectral region 1980–2300 Å.

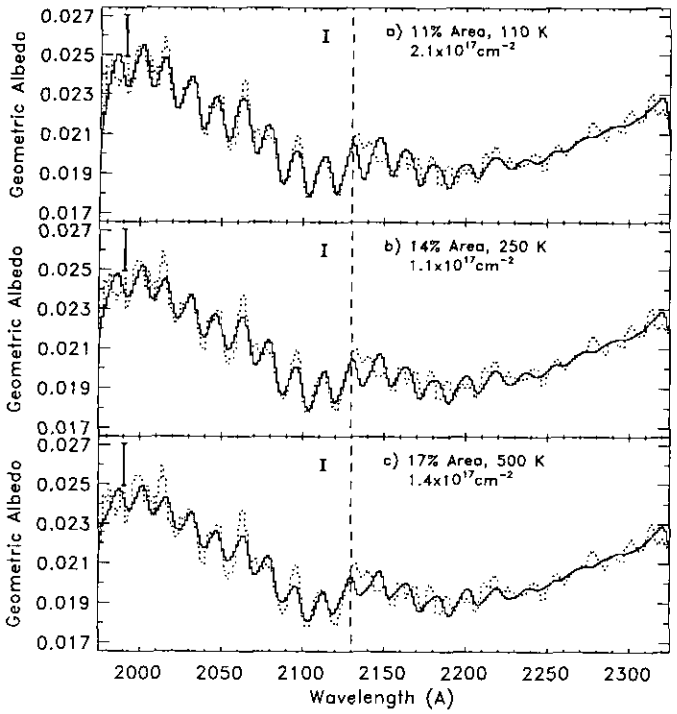

FIG. 11. Comparison between best fit models of spatially confined atmospheres at different temperatures. (a) 110 K, ~11% coverage. (b) 250 K, ~14% coverage. (c) 500 K, ~17% coverage.

relevant properties of the models are listed in Table I. Results obtained with the nonweighted fitting method were similar, except that the fitted column densities were lower by less than a factor of 2. Figures 9, 11, 12, and 13, showing results from the weighted fits, have vertical lines drawn at 2130 Å to visually separate the diagnostic regions.

2. *Results*

a. Column density, spatial distribution, and temperature. Three parameters in the models of Io's SO_2 atmosphere determine the overall intensity, contrast, and shape of the absorption bands, and consequently how well a model atmosphere albedo fits the HST data: they are the column density, temperature, and spatial distribution of the atmospheric SO_2. Since the reflected sunlight samples the whole atmospheric column down to the surface layers and our models are not multilayered, the model temperatures represent vertically averaged or effective temperatures. We tested the role of these three parameters in producing the observed albedo in the following manner. For each model atmosphere at a given temperature and spatial distribution, the SO_2 atmospheric column density was treated as a free parameter, finding the value (over several decades in density) yielding the best fit to the data. The results for different combinations of temperature and spatial distribution were then compared to find which combinations fit the data best. The effect of the temperature was modeled with atmospheres at average temperatures of 110, 250, and 500 K, ranging from the cold surface temperatures on Io to the hot values derived from the millimeter SO_2 observations. The spatial distributions were varied as follows: (i) the most general case of hemispherical (100%) coverage; (ii) a ±30° latitudinal band covering about 50% of the hemisphere and overlapping the main volcanic and frost areas; (iii) an atmosphere weighted by the possible SO_2 frost distribution visible as white patches in the Voyager images (McEwen *et al.* 1988) with an approximate 35% areal coverage in the trailing hemisphere; and (iv) more localized atmospheres at the subsolar point with hemispheric areal coverages decreasing down to ~5% (these can be alternatively placed at different locations compensating for the projected areas and air masses). Note that we are referring to hemispheric areal coverages and that the projected areas are larger.

We begin with the results for the most general case of a hemispheric atmosphere. For this case the average atmospheric temperature was varied from 110 to 500 K in more detailed ~50 K steps. Better fits are obtained for 200 and 250 K, with comparable fits for the range 150–300 K (Table I). The temperature of 250 K was chosen as as

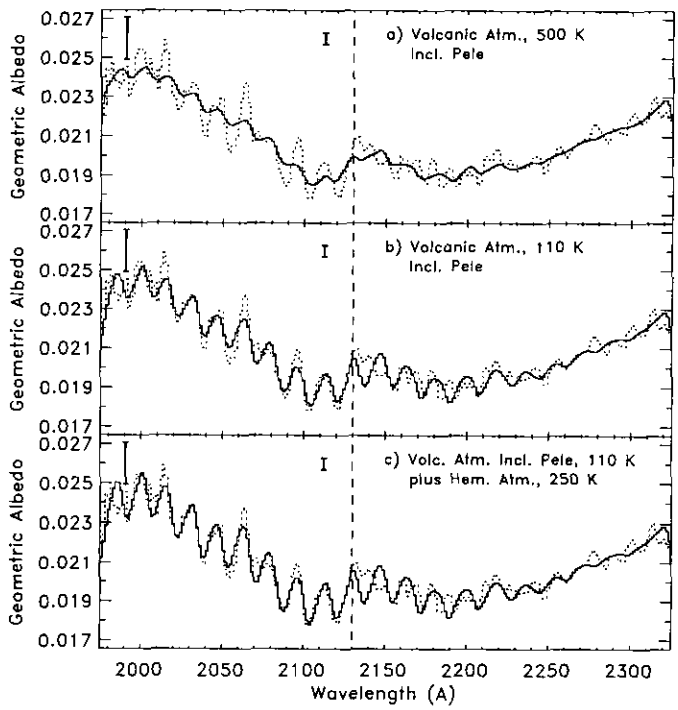

FIG. 12. Comparison of volcanic cases. (a) T_{volcs} = 500 K; Pele is included and model volcanic densities have been scaled by 0.1. (b) T_{volcs} = 110 K; Pele is included and model volcanic densities have been scaled by 0.3. (c) Two-component atmosphere combining the volcanic atmosphere in (b) with a hemispheric atmosphere at 250 K and $N = 1.4 \times 10^{15}$ cm^{-2}.

the mid-value for the other spatial fits to the data. Figure 9 shows the results for the hemispheric atmosphere at T = 110, 250, and 500 K, where one can see the subtle changes in the skewness, peak position, and contrast of the bands with temperature (the 110 K model has too high contrast around 2000 Å and the bands are not skewed enough, while the 500 K model bands have too much skewness). (To verify that the smoothing of the data is not influencing this result, the fits were also made using unsmoothed data, and we found the same temperature dependence with slightly higher column densities). The fitted hemispheric SO_2 column densities are in the range 6–10 $\times$ 10^{15} cm^{-2} for temperatures of 110–500 K. These column densities are still in the collisionally thick ($\mathcal{N} > 3 \times 10^{14}$ cm^{-2}) regime but are significantly lower than the previous IUE upper limit of 2 $\times$ 10^{17} cm^{-2} (Ballester *et al.* 1990).

As the spatial coverage of the atmosphere is reduced the fits improve for smaller areal coverages, and thus higher densities, with better fits at the colder gas temperature of 110 K. This result is presented in Fig. 10a, showing the weighted $\chi^2/102$ for the region 1980–2130 Å versus spatial coverage for the three atmospheric temperatures chosen (we also show the fitted SO_2 column densities). For a given atmospheric temperature, there is a turning point in the coverage at ~11, ~14, and ~17%, respectively, for 110, 250, and 500 K, above which the fits start to degrade because the contrast becomes too low due to the diminishing contribution of a shrinking area to the disk-integrated albedo. The fitted model albedos for these smallest coverages attainable at the three different temperatures are shown in Fig. 11. Note that with T = 110 K the localized 11% case gives a better fit below 2130 Å compared to the hemispheric case because the spectral contrast around 2000 Å is now at the correct level, and the shape of the resulting bands is improved, for example in the region around 2100 Å. Figure 10b shows the behavior of the sum of squared differences for the region above 2130 Å corresponding to the best fit found below 2130 Å: the increased densities for areal coverages smaller than ~35% give higher contrast in this region, and when the area becomes less than ~14% the contribution to the albedo is small and the contrast again decreases. Because the errors are undetermined in this region, it is hard to set a rigorous upper limit to acceptable contrast. The sum of squared differences for the whole spectral region is presented in Fig. 10c, showing the same general trend that was found for the region below 2130 Å.

b. Volcanic atmospheres. Localized, dense atmospheric regions associated with active volcanoes may be present on Io, as evidenced by the Voyager IRIS detection. Unlike the small areal coverage atmospheres studied above, a volcanic atmosphere would have different densities associated with each of the volcanoes. The uncertainties in the model volcanic atmosphere include the following characteristics for each volcano: (i) the activity at the time of the observation, in particular that of Pele, (ii) the relative SO_2 output, (iii) the effective gas temperature, (iv) the strength, and (v) the extent of the SO_2 column surrounding the volcano. We used a simple model for a volcanic atmosphere, described in Ballester *et al.* (1990), in which the model of the Loki plume by Ingersoll (1989), with a pressure of 2.2 $\times$ 10^{-8} bars over an area 300 km in radius, is scaled to other possible plume areas found by Strom *et al.* (1981) from Voyager images. In addition to the long-lived Loki volcano and other smaller volcanoes, we have also included Pele, which is Io's largest volcano but is sporadic, short-lived, and may not be mainly SO_2-driven (McEwen and Soderblom 1983). The resulting areal coverages and column densities are 73% for $\mathcal{N} \leq 10^{14}$, 4% for 10^{14}–10^{15}, 9% for 10^{15}–10^{16}, 5% for 10^{16}–10^{17}, 4% for 10^{17}–10^{18}, and 5% for 10^{18}–3.3 $\times$ 10^{18} cm^{-2}. There are many assumptions in this model, but the purpose is to make a reasonable representation of Io's volcanic SO_2 atmospheric component and test the effect on the data. We used volcanic gas temperatures of 110, 150, 250, and 500 K, and we also scaled the volcanic column densities, and thus the volcanic strength, over 5 decades in density.

When Pele is excluded from the model, the volcanic atmosphere is too confined to give enough spectral contrast below 2130 Å for either cold or hot temperatures, even when adjusting the volcanic densities.

When Pele is included, the results are sensitive to the temperature of the gas. At 150–500 K temperatures the spectral contrast is still too small to fit the data even with scaled volcanic densities. Figure 12a shows the fit at 500 K. Only at the coldest 110 K temperature does the contrast increase sufficiently to yield almost a good fit and then only when the volcanic densities are scaled by a factor of ~0.3 (at larger densities saturation effects decrease the spectral contrast). This fit is shown in Fig. 12b. Above 2130 Å the contrast is somewhat large, as in the small-area cases discussed above, but we do not have a method of constraining the contrast in this region. Because Pele is the dominant volcano, the scaling of the volcanic densities reflects mainly the scaling of its output. We have already found that the other volcanoes could have higher densities and still agree with the HST data. The results at the cold temperatures are quite sensitive to the spatial extent assumed for the volcanic atmosphere, and within the uncertainties of the model, it is possible that a somewhat larger Pele model could give a good fit to the data.

c. Two-component atmospheres. Io's atmosphere has different sources of SO_2 which may result in atmospheric components of different average properties. We have

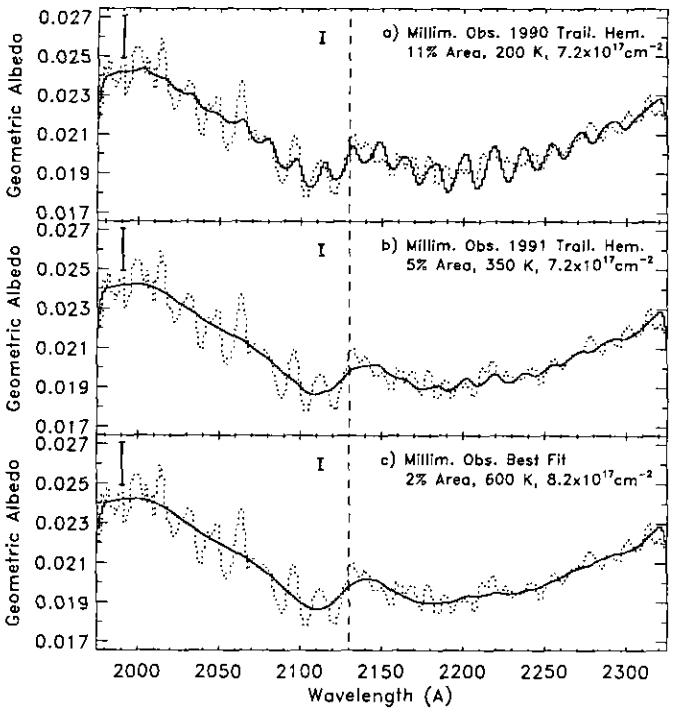

FIG. 13. Comparison with results from millimeter data by Lellouch *et al.* (1990) (see text). (a) 1990 Trailing hemisphere. (b) 1991 Trailing hemisphere. (c) Best fit for all their millimeter data combined.

therefore tested a simple two-component model combining the dense, patchy volcanic-like atmospheres with hemispheric atmospheres representing a tenuous, more extended component. Most model volcanic atmospheres were shown to give insufficient spectral contrast in the SO_2 bands below 2130 Å and thus require an additional atmospheric component to fit the HST data. The two-component model was constructed according to (i) use of the volcanic component wherever its density exceeded the hemispheric value; (ii) treatment of the hemispheric column density as a free parameter; and (iii) use of hemispheric temperatures fixed at 110, 250, and 500 K. In the cases that include Pele, the volcanic densities have been scaled down by the factors found above the one-component volcanic atmospheres to fit the data best (0.3, 0.1, and 0.1, respectively, for volcanic temperatures of 110, 250, and 500 K).

In all cases, the fits are improved over the separate one-component volcanic and hemispheric atmospheres, and even more so when the volcanic temperature is 110 K. The cases combining the cold 110 K volcanic atmosphere that includes Pele give very good fits to the data as shown in Fig. 12c. Because the one-component volcanic models produce relatively little contrast, the results obtained in the two-component models follow those of the hemispheric atmospheres in that the warm 250 K hemispheric temperature give better fits (the dependence is marginal with the cold 110 K volcanic atmosphere that includes Pele). The fitted hemispheric densities are in the 10^{15}–10^{16} cm^{-2} regime, reduced from the one-component hemispheric densities by factors of ~0.2–0.9.

Finally, some of the two-component models were also tested by combining the volcanic atmospheres with the hemispheric atmosphere weighted by the distribution of SO_2 frost, a patchy SO_2 atmospheric component that could for example be generated locally by sublimation of SO_2 frost. The results were very similar to those obtained with the hemispheric atmosphere except with larger fitted column densities (by factors of ~2–3). In general, we also infer that combining a volcanic component with an atmosphere of reduced areal coverage, as discussed in Section 2a, would yield cases which fit the data well.

d. Comparison with millimeter SO_2 observations. The single-component analysis of the millimeter-wave observations made by Lellouch *et al.* (1992) gives very specific, although nonunique, results which we have also compared with the HST data. Their best fit cases (cited in their Fig. 6) include: the best fit for the whole set of observations of a volcano-like atmosphere, with $\mathcal{N} = 8.2 \times 10^{17}$ cm^{-2}, ~2% areal coverage and 600 K temperature; the fit for the trailing hemisphere for 1991 data with $\mathcal{N} = 7.2 \times 10^{17}$ cm^{-2}, ~5% areal coverage, and $T = 350$ K; and the fit for 1990 trailing data with the same density as in 1991 but with a more extended ~11% coverage and $T = 200$ K. (These areal coverages at the subsolar point correspond, respectively, to the ~5, 9, and 22% projected areas quoted by Lellouch *et al.*). We found that none of these model atmospheres fits our HST data, as shown in Fig. 13. The best fit and 1991 atmospheres covering, respectively, ~2 and 5% of the surface (Figs. 13c, b) have no contrast below 2130 Å, as one can infer from the minimum acceptable areal coverages of 11–17% illustrated in Fig. 11. In the limit of the higher column densities required by Lellouch *et al.* (1992) saturation effects in the SO_2 UV bands are significant and further degrade the already low contrast due to small areal coverage. The single exception is for the 1990 trailing hemisphere (Fig. 13a) where the areal coverage is 11%. Although this area is sufficiently large, the density is too high by about a factor of 5: saturation occurs below 2130 Å, but not above 2130 Å, where the resultant atmospheric SO_2 band absorption signature is unacceptably large. However, this millimeter observation had the worst S/N, and the best fit model atmosphere of Lellouch *et al.* (1992) also fits this data. (The best fit model does not exhibit detectable bands above 2130 Å, Fig. 13c.) Therefore, the millimeter-wave inferred atmospheres are invisible in the ultraviolet due to small areal coverage and saturation of the HST detected SO_2 bands.

e. Fluorescence. Finally, another aspect we had to consider for the region above 2130 Å was the strong fluorescence known to occur in SO_2 for bands above the predissociation threshold at ~2200 Å, with peak quantum efficiencies ranging from 100 to 40% in the 2200- to 2325-Å region (Okabe 1971, Ahmed and Kumar 1992). This fluorescence is not quenched in Io's tenuous atmosphere. We do not have information on what percentage of photons is reemitted within the same band because the measured quantum efficiencies encompassed large bandpasses: if it were 100%, we would see quite a different signature in the albedo, with emission instead of absorption at the bands. We constructed a model for the geometric albedo including the fluorescence with a scaling factor to estimate the maximum possible contribution. The model included single scattering albedo (valid for an optically thin case) in the incident and reflected beams. We found that the maximum fluorescence contribution may be ~20%. Some cases with 5 or 10% fluorescence give slightly better fits in the region above 2130 Å, but as in the case of pure absorption, the model looks out of phase with the data, particularly for the strongest band at 2207 Å.

V. SUMMARY AND CONCLUSIONS

The SO_2 absorption signature in the UV albedo of Io's trailing hemisphere observed with HST provides constraints on the density, temperature, and spatial distribution of the SO_2 atmosphere even though the disk-integrated HST data cannot resolve the spatial distribution. A hemispheric atmosphere fits the data well with average column density $\mathcal{N} = 6\text{–}10 \times 10^{15}$ cm^{-2} for temperatures in the 110–500 K range. More spatially confined atmospheres yield better fits, with a limit of ~8% areal coverage and ~3×10^{17} cm^{-2} column density. The uncertainty in the derived densities is better than a factor of 2. These moderate densities are on average 10–30 times less dense than the IUE upper limit, and are also smaller than inferred from millimeter-wave observations.

A localized and dense ($\mathcal{N} \geq 10^{16}$ cm^{-2}) SO_2 atmosphere, as could be associated with the volcanoes on Io, cannot generate the observed spectral contrast regardless of the atmospheric temperature (110–500 K), unless the Pele volcano is included with a cold (110 K) atmosphere. Whereas most model volcanic SO_2 atmospheres could be present, an additional atmospheric component is required to fit the HST data. Two-component models which combine volcanic-like atmospheres with a hemispheric component, or one weighted by the SO_2 frost distribution, significantly improve the fits, with the coldest volcanic-component temperatures giving the best fits.

The millimeter-wave data obtained by Lellouch *et al.* (1992) were best fitted with localized SO_2 component of ≤5% areal coverage which gives a spectral contrast too weak to fit the HST data. To reconcile the data sets, one can, in principle, add a millimeter-wave atmosphere with areal coverage ≤5% to one of the cold (T = 110 K) atmospheres given in Table I and obtain an acceptable two-component model which would fit both the HST and millimeter-wave observations, because the latter is a measurement of relative temperature contrast with the ground. A detailed comparison of the HST and millimeter data is currently underway.

In terms of the atmospheric temperature, the hemispheric atmosphere fits better with warm 150–300 K average temperatures, but as the areal coverage decreases the data fit better with colder temperatures. This is also true for volcanic atmospheres. If these results are confirmed with better S/N data, the preference found for localized, dense atmospheres that are cold (~110 K) is consistent with the calculations of the vertical temperature structure of Io's atmosphere by Strobel *et al.* (1994), who found that when the surface pressure exceeded 10 nbar the atmosphere became quasi-isothermal at the surface temperature to a pressure of 1 nbar and with the formation of a mesopause region somewhere between the surface and 1 nbar. However, the millimeter-wave observations have been interpreted to be emission from an isothermal 600 K atmosphere with most of the line formation occurring in the 1- to 16-nbar region.

It may be possible to reconcile this discrepancy by noting that the intrinsic rotational line Doppler width is ~900 K, which corresponds to a characteristic velocity of ~0.5 km sec^{-1}. This velocity is also typical of the initial injection velocities of most volcanic plumes detected by Voyager imaging (Strom and Schneider 1982), with only a few plumes having velocities that equal or exceed 1 km sec^{-1}. The essential question lies with the relative contributions to the overall line shape by (1) thermal broadening and (2) Doppler components of expanding volcanic plume gases. This topic is currently under investigation.

If the moderate SO_2 atmospheric densities found with HST are at least partly produced by sublimation of the surface SO_2 frost, the results imply an average effective temperature of sublimation ranging from 108 to 110 K for the hemispheric cases to 118 K for the smallest areal coverages. This temperature regime is low compared to most temperature distributions previously studied for Io. Since the surface frost must undergo some degree of heating and thus sublimation during the day, our results imply that there may be processes reducing the sublimation that would result from standard temperature models. Processes that reduce the effective temperature of the SO_2 frost (such as an insolation–propagation mechanism; Brown and Matson 1987) may require further study. Another aspect of the sublimation process that is not clear is whether SO_2 frost intimately mixed with other frosts,

as strongly suspected to occur on Io (Howell *et al.* 1984, McEwen *et al.* 1988), follows the vapor-pressure curve of pure SO_2 frost reported by Wagman (1979). A lower vapor-pressure curve, for example, would result in higher average frost temperatures than found above. On the other hand, it is always possible that the SO_2 frost abundance was low at the time of the HST observations in March 1992, since it must be ultimately maintained by the volcanoes which may have had particularly low activity: Johnson *et al.* (1992) report that disk-integrated thermal fluxes of the trailing hemisphere made 1 month before our HST observations were the lowest observed since 1983, and Spencer *et al.* (1992) report that the dominant Loki volcano resolved in ProtoCam images was quiet between October 1991 and May 1992. Further observations are required to study the relationship of Io's volcanic activity and its SO_2 atmospheric abundance, whether through direct volcanic output or related sublimation sources. The moderate densities found for the SO_2 atmosphere, whether patchy or global, may also have implications on the interaction of the plasma torus with the atmosphere and surface (Johnson 1989). The atmospheric SO_2 will be more exposed to the torus plasma (unless other unidentified atmospheric components are more abundant) and may thus be more efficiently heated and more efficiently removed from the atmosphere in molecular form, and the surface may also be exposed to the torus bombardment during the day.

ACKNOWLEDGMENTS

We gratefully acknowledge the staff at STScI for assistance in the acquisition and reduction of the data, C. Cunningham for providing calibrated FOS and HRS spectra of 16-Cygni in digital form, M. VanHoosier for providing the solar spectra as well as J. Lean for helpful conversations on the solar spectrum, and J. Joens and the staff at NSSDCA for providing SO_2 absorption data in digitized form. We also thank J. Clarke and H. Weaver for helpful discussions on the data acquisition and analysis. We thank E. Lellouch for useful suggestions and discussions about the millimeter-wave observations of Io. We are also most grateful to M. Belton for critical and valuable review of the paper. Support for this work was provided by NASA through a grant from the Space Telescope Science Institute, which is operated by AURA, Inc., under NASA Contract NAS 5-26555. D.F.S. and X.Z. were partially supported by NASA Grant NAGW-648 in the modeling effort associated with this research. A portion of D.F.S. research was accomplished at the Observatoire de Paris—Meudon. He thanks the Departement de Recherche Spatiale for its hospitality and CNRS for its support. G.E.B. acknowledges partial support by NASA Grant NAGW-1766 to the University of Michigan.

REFERENCES

AHMED, S. M., AND V. KUMAR 1992. Quantitative photoabsorption and fluorescence of SO_2 at 188–231 and 278.7–320 nm. *J. Quant. Spectrosc. Rad. Transfer* **47,** 359–373.

ANDERSON, G. P., AND L. A. HALL 1989. Solar irradiance between 2000 and 3100 Angstroms with spectral band pass of 1.0 Angstroms. *J. Geophys. Res.* **94,** 6435–6441.

BALLESTER, G. E., D. F. STROBEL, H. W. MOOS, AND P. D. FELDMAN 1990. The atmospheric abundance of SO_2 on Io. *Icarus* **88,** 1–23.

BELTON, M. J. S. 1982. An interpretation of the near-ultraviolet absorption spectrum of SO_2. Implications for Venus, Io, and laboratory measurements. *Icarus* **52,** 149–165.

BLAIR, W. P., A. F. DAVIDSEN, AND A. UOMOTO 1989. Scattered red light in the FOS. *Instrument Science Report CAL/FOS-058.* Johns Hopkins University.

BROWN, R. A., AND D. L. MATSON 1987. Thermal effects of insolation propagation into the regoliths of airless bodies. *Icarus* **72,** 84–94.

CLARKE, J. T., J. AJELLO, J. LUHMAN, N. SCHNEIDER, AND I. KANIK 1994. HST UV spectral observations of Io passing into eclipse. *J. Geophys. Res. Planets* **99**(E4), 8387–8407.

COLLINS, S. A. 1981. Spatial color variations in the volcanic plume at Loki, on Io. *J. Geophys. Res.* **86,** 8621–8626.

FANALE, F. P., W. B. BANERDT, L. S. ELSON, T. V. JOHNSON, AND R. W. ZURICK 1982. Io's surface: Its phase composition and influence on Io's atmosphere and Jupiter's magnetosphere. In *Satellites of Jupiter* (D. Morrison, Ed.), pp. 756–781. Univ. of Arizona Press, Tucson.

FREEMAN, D. E., K. YOSHINO, J. R. ESMOND AND W. H. PARKINSON 1984. High resolution absorption cross section measurements of SO_2 at 213 K in the wavelength region 172–240 nm. *Planet. Space. Sci.* **32,** 1125–1134.

GOODY, R. M., AND Y. L. YUNG 1989. *Atmospheric Radiation: Theoretical Basis,* 2nd Ed. Oxford Univ. Press, New York and Oxford.

HAPKE, B. W., E. WELLS, J. WAGNER, AND W. PARTLOW 1981. Far-UV, visible, and near-IR reflectance spectra of frosts of H_2O, CO_2, NH_3, and SO_2. *Icarus* **47,** 361–367.

HOWELL, R. R., D. P. CRUINSHANK AND F. P. FANALE 1984. Sulfur dioxide on Io: Spatial distribution and physical state. *Icarus* **57,** 83–92.

INGERSOLL, A. P. 1989. Io meteorology: How atmospheric pressure is controlled locally by volcanos and surface frosts. *Icarus* **81,** 298–313.

INGERSOLL, A. P., M. E. SUMMERS, AND S. G. SCHLIPF 1985. Supersonic meteorology of Io: Sublimation-driven flow of SO_2. *Icarus* **64,** 375–390.

JOHNSON, R. E. 1989. Plasma heating of an SO_2 atmosphere on Io. *Geophys. Res. Lett.* **16,** 1117–1120.

JOHNSON, T. V., D. L. MATSON, D. L. BLANEY, G. J. VEEDER AND J. D. GOGUEN 1992. Ground based observations of the temporal and spatial variations in the heat flow of Io. *Time Variable Phenomena in Jovian Systems,* July 1992, Annapolis, MD.

KINNEY, A. L. 1992. *Faint Object Spectrograph Instrument Handbook, Version 2.0.* Space Telescope Science Institute, Baltimore.

LACIS, A. A., AND V. OINAS 1991. A description of the correlated k distribution method for modeling nongray gaseous absorption, thermal emission, and multiple scattering in vertically inhomogeneous atmospheres. *J. Geophys. Res.* **96**(D5), 9027–9063.

LEAN, J. 1987. Solar ultraviolet irradiance variations: A review. *J. Geophys. Res.* **92,** 839–868.

LELLOUCH, M. BELTON, I. DE PATER, S. GULKIS, AND T. ENCRENAZ 1990. Io's atmosphere from microwave detection of SO_2. *Nature* **346,** 639–641.

LELLOUCH, M. BELTON, I. DE PATER, G. PAUBERT, S. GULKIS, AND T. ENCRENAZ 1992. The structure, stability, and global distribution of Io's atmosphere. *Icarus* **98,** 271–295.

MARTINEZ, R. D., AND A. JOENS 1992. SO_2 absorption cross-section measurements from 197 nm to 240 nm. *Geophys. Res. Lett.* **19,** 277–279.

MATSON, D. L., AND D. B. NASH 1983. Io's atmosphere: Pressure control by regolith cold trapping and surface venting. *J. Geophys. Res.* **88,** 4771–4783.

McEwen, A. S., and L. A. Soderblom 1983. Two classes of volcanic plumes on Io. *Icarus* **55,** 191–217.

McEwen, A. S., T. V. Johnson, D. L. Matson, and L. A. Soderblom 1988. The global distribution, abundance, and stability of SO_2 on Io. *Icarus* **75,** 450–478.

McGrath, M. A., and R. E. Johnson 1987. Magnetospheric plasma sputtering of Io's atmosphere. *Icarus* **69,** 519–531.

Moreno, M. A., G. Schubert, J. Baumgardner, and M. G. Kivelson 1991. Io's volcanic and sublimation atmospheres. *Icarus* **93,** 450–478.

Nash, D. B., F. P. Fanale, and R. M. Nelson 1980. SO_2 frost: UV–visible reflectivity and Io surface coverage. *Geophys. Res. Lett.* **7,** 665–668.

Nash, D. B., M. H. Carr, J. Gradie, D. M. Hunten, and C. F. Yoder 1986. Io. In *Satellites* (J. Burns and M. S. Matthews, Eds.), pp. 629–688. Univ. of Arizona Press, Tucson.

Okabe, H. 1971. Fluorescence and predissociation of sulfur dioxide. *J. Am. Chem. Soc.* **93,** 7095–7096.

Paresce, F., P. Sartoretti, R. Albretch, C. Barbieri, J. C. Blades, A. Boksenberg, P. Crane, J. M. Deharveng, M. J. Disney, P. Jakobsen, T. M. Kamperman, I. R. King, F. Machetto, C. D. Makey, G. Weigelt, D. Baxter, P. Greenfield, R. Jedrzejewski, A. Nota, and W. B. Sparks 1992. Near UV imaging of Jupiter's satellite Io. *Astron. Astrophys.* **262,** 617–622.

Pearl, J. C., R. Hanel, V. Kunde, W. Maguire, D. Fox, S. Gupta, C. Ponnamperuma, and F. Raulin 1979. Identification of gaseous SO_2 and new upper limits for other gases on Io. *Nature* **280,** 755–758.

Sartoretti, P., M. A. McGrath, and F. Paresce 1944. Disk-resolved imaging of Io with the Hubble Space Telescope. *Icarus* **108,** 272–284.

Simonelli, D. P., and J. Veverka 1986. Disk-resolved photometry of Io. I. Near opposition limb darkening. *Icarus* **66,** 403–527.

Sirk, M., and R. Bohlin 1985. Scattered red light. *Space Telescope Science Institute FOS Instrument Science Report CAL/FOS-013.*

Spencer, J. R., B. E. Clark, D. O'Connor, and W. M. Sinton 1992. Variability of thermal emission from individual Io hot spots, 1989–1992. *Time Variable Phenomena in Jovian Systems,* July 1992, Annapolis, MD.

Strobel, D. F., X. Zhu, and M. E. Summers 1994. On the vertical thermal structure of Io's atmosphere. *Icarus* **111,** 18–30.

Strom, R. G., N. M. Schneider, R. J. Terrile, A. F. Cook, and C. Hansen 1981. Volcanic eruptions on Io. *J. Geophys. Res.* **86,** 8593–8620.

Strom, R. G., and N. M. Schneider 1982. Volcanic eruption plumes on Io. In *Satellites of Jupiter* (D. Morrison, Ed.), pp. 598–633. Univ. of Arizona Press, Tucson.

VanHoosier, M. E., J.-D. F. Bartoe, G. E. Brueckner, and D. K. Prinz 1988. Absolute solar spectral irradiance 120 nm–400 nm (results from the Solar Ultraviolet Spectral Irradiance Monitor-SUSIM-Experiment on board Spacelab 2). *Astron-Lett. Commun.* **27,** 163–168.

Wagman, D. D. 1979. *Sublimation Pressure and Enthalpy of SO_2.* Chemical Thermodynamics Data Center, National Bureau of Standards, Washington, DC.

Zhu, X. 1988. An improved Voigt line approximation for the calculations of equivalent width and transmission. *J. Quant. Spectrosc. Radiat. Transfer* **39,** 421–427.

Zhu, X., 1991. Spectral parameters in band models with distributed line intensity. *J. Quant. Spectrosc. Radiat. Transfer* **45,** 33–46.

Zhu, X., 1992. The correlated-k coefficients calculated by random band models. *J. Quant. Spectrosc. Radiat. Transfer* **47,** 159–170.

Zhu, X., 1994. An accurate and efficient radiation algorithm for middle atmosphere models. *J. Atmos. Sci.,* in press.